AIMS Materials Science, 13(5): 976–995.
DOI: 10.3934/matersci.2026046
Received: 20 June 2026
Revised: 12 September 2026
Accepted: 08 October 2026
Published: 05 November 2026

https://www.aimspress.com/journal/Materials

Research article

Beyond traditional brittleness: A novel post-peak ductility index (PDI) for assessing fracture energy in eco-friendly hybrid concretes

Grzegorz Ludwik Golewski*

Department of Structural Engineering, Faculty of Civil Engineering and Architecture, Lublin University of Technology, Nadbystrzycka 40 str., 20-618, Lublin, Poland

* **Correspondence:** Email: g.golewski@pollub.pl; Tel: +48-81-5384394; Fax: +48-81-5384390.

Abstract: The development of sustainable structural concrete increasingly incorporates supplementary cementitious materials (SCMs) and nanoadditives to drastically reduce carbon footprints. However, microstructural densification using nanosilica (NS) and silica fume (SF) often enhances compressive strength at the expense of increased structural brittleness. Traditional engineering methods evaluate this brittleness through empirical static strength ratios (e.g., the brittleness index, *BI*), which inherently fail to reflect the post-cracking energy dissipation mechanisms and non-linear softening behavior. To overcome this limitation, we introduced a novel energy-based metric designated as the post-peak ductility index (*PDI*), which mathematically isolates the post-peak energy (W_{post}) relative to the total work of fracture (W_t). An extensive experimental campaign was conducted on four distinct concrete formulations: a 100% ordinary Portland cement (OPC), reference concrete (REF), a ternary nano-composite (NSF, containing 5% NS and 10% SF), and two quaternary hybrid systems combining 5% NS, 10% SF, and varying contents of fly ash (FA) (5% and 15% FA) (quaternary hybrid concretes: H1 and H2). The holistic mechanical and fracture performance was characterized via three-point bending tests on notched beams, coupled with advanced multi-criteria radar chart mapping and Pearson correlation matrix analysis. The experimental results demonstrated a beneficial interaction in the quaternary formulation H1, which achieved a 48% increase in compressive strength alongside a 145% explosion in the W_t (W_t = 2.012 J) compared to the REF concrete. Furthermore, while the sole addition of NS increased matrix brittleness (reducing *PDI* to 85.01%), the inclusion of FA successfully restored ductility (*PDI* up to 89.71%). Statistical validation confirmed that the classical *BI* correlates negatively with actual fracture work, proving its inadequacy for high-performance formulations, whereas the proposed *PDI* accurately tracks true non-linear structural safety margins.

Keywords: post-peak ductility index (*PDI*); brittleness index (*BI*); quaternary hybrid concrete; siliceous fly ash (FA); silica fume (SF); nanosilica (NS); non-linear fracture mechanics; softening behavior; total fracture energy (G_f); multi-criteria evaluation

1. Introduction

The development of modern sustainable construction materials demands a paradigm shift toward minimizing the carbon footprint of cementitious composites while maintaining or enhancing their mechanical and durability performance [1–4]. Ordinary Portland cement (OPC) production remains one of the primary industrial sources of carbon dioxide emissions globally [5–8]. To mitigate this environmental burden, the binary, ternary, and quaternary blending of cement [9–12] using supplementary cementitious materials (SCMs) [13–15], such as fly ash (FA) [16,17] and silica fume (SF) [18–20], has become standard practice [21,22]. Concurrently, the integration of nanotechnology, particularly nanosilica (NS) [23–26], has emerged as a powerful strategy to accelerate early-stage hydration [27,28], densify the interfacial transition zone (ITZ) [29–31], and promote the formation of additional calcium silicate hydrate (C-S-H) gels via high-reactivity pozzolanic reactions [32–35].

However, the modification of concrete microstructures using SCMs and nanoadditives [36–38] significantly alters the macro-mechanical response of the material [39–42]. While the hybrid effects of combining nano- and micro-fillers often lead to significant increases in compressive and tensile strengths, they frequently induce higher structural brittleness [43,44]. Moreover, brittle materials are prone to sudden, catastrophic failure under peak loading scenarios, which poses severe risks to structural integrity [45–47]. Traditionally, the brittleness of concrete has been evaluated using empirical indices, such as the brittleness index (*BI*), derived purely from the ratios of static strength parameters (e.g., splitting tensile strength to compressive strength) [48–50]. Although these index-based approaches provide quick engineering estimates, they fail to capture the post-cracking energy dissipation mechanisms, the softening behavior, and the true fracture toughness of the matrix [51–53]. As established in our comprehensive evaluation of eco-friendly cementitious composites published in *AIMS Materials Science*, a deeper, multiscale analysis incorporating advanced fracture mechanics criteria is imperative to accurately characterize the structural reliability of modified concrete formulations [54].

To overcome the limitations of classic strength-based indicators, non-linear fracture mechanics based on the Three-Point Bending Test (TPBT) of notched beams offers an accurate framework [55–57]. Parameters such as the critical stress intensity factor (K_{Ic}^{S}), critical crack tip opening displacement ($CTOD_c$), and total fracture energy (G_f) provide fundamental insights into crack propagation resistance [58–61]. Nonetheless, evaluating the absolute values of fracture work does not explicitly isolate the material's post-peak ductility in a standardized [62,63], relative manner [63–66]. To address this research gap, we introduce a novel energy-based parameter designated as the post-peak ductility index (*PDI*). The *PDI* explicitly quantifies the proportion of energy absorbed during the stable and unstable macro-crack propagation phase (post-peak energy, W_{post}) relative to the total work of fracture (W_t), thereby providing an absolute indicator of post-cracking structural safety and toughness [67–69].

Our primary objective of this paper is to investigate the hybrid efficiency of ternary and quaternary cementitious matrices modified with NS, SF, and varying contents of FA under classic strength criteria [70,71] and advanced fracture mechanics parameters [72–74]. Our scope of the study

encompasses the comprehensive testing of four distinct concrete mix designs: a 100% OPC reference concrete (REF), a ternary nano-composite (NS + SF) (NSF), and two quaternary hybrid formulations containing low and high volumes of FA (quaternary hybrid concretes: H1 and H2). Rather than relying on isolated parameters, this work implements an advanced multi-criteria evaluation via normalized radar chart mapping and Pearson correlation matrix analysis as exploratory descriptive analysis. This comprehensive statistical and graphical approach isolates the explicit relationships between conventional *BI* [54] and the newly proposed *PDI*, establishing a robust methodology for the design of highly ductile, sustainable structural concretes.

While classical parameters such as ASTM C1018 toughness indices or absolute residual strength measures evaluate general energy absorption, they often rely on deflection measurements that include bulk specimen and support deformations. The novelty of the proposed *PDI* lies in its strict coupling with the Crack Mouth Opening Displacement (*CMOD*). By evaluating the ratio of post-peak work to total work derived directly from the load–*CMOD* response, the *PDI* isolates the localized fracture process zone. This provides a simplified, normalized measure of the material's intrinsic crack-bridging capability, independent of external elastic compliance artifacts, thus offering genuinely new insights into the transition from brittleness to ductility in hybrid concretes. Moreover, it should be noted that while plain concrete fundamentally exhibits quasi-brittle softening, the term "ductility" within the *PDI* framework is utilized as an operational descriptor for enhanced post-peak toughness and relative fracture resistance.

2. Materials and methods

2.1. Experimental setup

The systematic experimental campaign executed in this study is visually structured and summarized in the comprehensive research flowchart presented in Figure 1. The methodology progressed sequentially from raw materials characterization and precise mix design formulation of green concretes, through specimens molding and standardized curing protocols, to parallel destructive mechanical testing tracks and integrated multi-criteria data processing.

However, while a full quantitative Life Cycle Assessment (LCA) was beyond our scope of this fracture mechanics study, the utilization of industrial by-products (FA, SF) as partial cement replacements aligned with the general principles of sustainable concrete design.

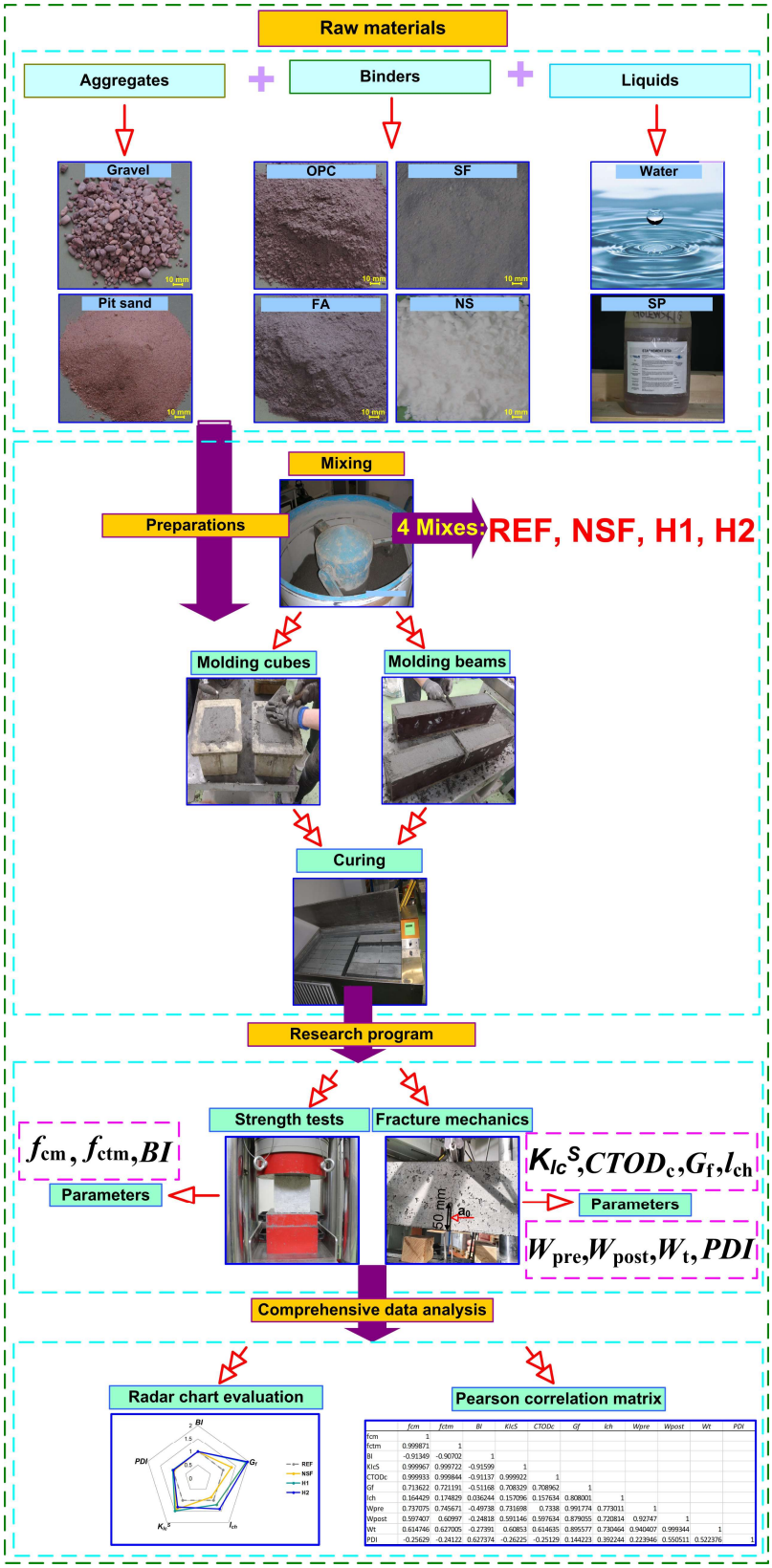


Figure 1. Flowchart of the experimental program: from raw materials selection (with incorporated scale bars for size reference) and specimen preparation to mechanical testing and comprehensive data analysis.

2.2. Materials and binder compositions

It should be clarified that the specific experimental matrix in this study was designed to evaluate the advanced fracture behavior of pre-selected, high-potential quaternary mixtures rather than to isolate the individual contributions of each SCM. Therefore, while full single- and dual-addition control groups were omitted from this specific fracture campaign, the mixtures represented combined formulations that demonstrated favorable mechanical performance in earlier compositional screening.

The primary binder used in this study was ordinary Portland cement (CEM I 32.5 R), conforming to EN 197-1:2011 [75]. To form the hybrid cementitious matrices, three distinct SCMs were utilized: FA [76], SF, and NS. These materials fundamentally differed in their physical properties. The gravities for OPC, FA, SF, and NS were: 3.11, 2.14, 2.21, and 1.10 g/cm^3, respectively. Concurrently, their specific surface areas (Blaine's fineness) varied significantly, highlighting the extreme fineness of the nanoadditive (0.33, 0.35, 1.40, and 200 m^2/g, respectively). Detailed chemical compositions and comprehensive physical parameters of all the applied constituents were thoroughly presented in the author's preceding study [54]. The OPC was primarily composed of CaO (approx. 63%) and SiO_2 (approx. 20%). The FA was mainly siliceous (SiO_2 > 50%, Al_2O_3 > 25%), while SF and NS were highly rich in amorphous silica (SiO_2 > 90% and > 99%, respectively). Regarding the fine aggregates, the clean pit sand utilized in the mixtures had a standard particle size fraction of 0–2 mm.

Four distinct concrete mixtures were designed with a constant water-to-binder (w/b) ratio of 0.40 to ensure direct comparative validity across all matrices [77]. The reference mix (REF) consisted of 100% OPC as the sole binding agent. The ternary mix (NSF) incorporated a combination of 85% OPC, 5% NS, and 10% SF by mass of the total binder content. To investigate the quaternary synergy, two hybrid mixes, designated as H1 and H2, were prepared by introducing FA as an additional cement replacement. Mix H1 contained 80% OPC, 5% NS, 10% SF, and 5% FA, while mix H2 evaluated a higher substitution rate consisting of 70% OPC, 5% NS, 10% SF, and 15% FA [78–81].

The aggregate mix was engineered using two distinct mineral groups, designed based on the guidelines of DIN 4226-1:2001-07 [82] and EN 13791:2019-12 [83]. High-quality gravel (maximum aggregate size of 8 mm) and clean pit sand were utilized as coarse and fine aggregates, respectively, maintained at identical proportions (1205 and 676 kg/m^3) across all four series to isolate the effects of binder modification. To maintain optimal workability and a uniform consistency across the modified series, a polycarboxylate-ether-based superplasticizer (SP) was added to the NSF, H1, and H2 mixtures. The detailed concrete specimen mixing proportions and ingredient mass ratios per cubic meter (kg/m^3) are compiled in Table 1.

Table 1. Concrete specimen mixing ratios (kg/m^3).

Mix	Mix No.	OPC	FA	SF	NS	Water	SP	Sand	Gravel
100% OPC	REF	352	0	0	0	141	0	676	1205
85% OPC + 0% FA + 10% SF + 5% NS	NSF	299.2	0	35.2	17.6	141	6	676	1205
80% OPC + 5% FA + 10% SF + 5% NS	H1	281.6	17.6	35.2	17.6	141	6	676	1205
70% OPC + 15% FA + 10% SF + 5% NS	H2	246.4	52.8	35.2	17.6	141	6	676	1205

2.3. Specimen preparations and curing

The concrete mixtures were prepared in a laboratory counter-rotating mixer following a multi-stage procedure to ensure homogeneous dispersion of the ultra-fine silica particles and FA grains. The fresh concrete mixtures were cast into steel molds in two subsequent layers, with each layer being fully compacted on a high-frequency vibrating table. Cube specimens measuring 150 × 150 × 150 mm were produced for basic mechanical testing (compressive strength, f_{cm} and splitting tensile strength, f_{ctm}), while notched beam specimens with dimensions of 80 × 150 × 700 mm were cast for fracture testing, strictly complying with the EN 12390-2:2019 guidelines [84]. During the casting of the beams, rigid steel inserts were precisely positioned to shape an initial pre-crack a_0 with a depth of 50 mm (Figure 1). This protocol successfully avoided post-hardening diamond-saw cutting, thereby protecting the crack tip zone from induced micro-damage (Figure 1). After casting into standard molds, the specimens were vibrated and covered with a damp cloth for 48 h at 20 ± 2 ℃. Following demolding, the elements were cured in a water tank for 14 days and maintained at a relative humidity ≥95% and a temperature of 20 ± 2 ℃, and then left in laboratory conditions until testing at 28 days of age (Figure 1).

2.4. Destructive testing protocols

Upon completing the curing regime, the cube specimens were subjected to destructive testing to determine the average f_{cm} and f_{ctm} in accordance with EN 12390-3 [85] and EN 12390-6 [86] standards, respectively. Using these primary mechanical parameters, the empirical *BI* was calculated to characterize the strength-based elasticity-to-tensile ratio (Figure 1). The analytical formulations governing these basic strength parameters are detailed in Table 2.

Table 2. Summary of analytical equations used for determining the main strength parameters.

Analysed parameter	Calculation equation	Reference
f_{cm}	$f_{cm} = \frac{F}{d^2}$	[85]
	where: F: the measured maximum load; d: the sample edge equal to 150 mm	
f_{ctm}	$f_{ctm} = \frac{2F}{\pi d^2}$	[86]
BI	$BI = \frac{f_{ctm}}{f_{cm}} \times 100\%$	[54]

The rectangular beam specimens were prepared for fracture mechanics characterization by forming a precise central initial crack at the mid-span using steel inserts during the specimen preparations procedure (Figure 1). The beams were tested under a closed-loop servo-controlled testing machine in a TPBT configuration over a: span (L) of 700 mm, clear span (S) of 600 mm; beam depth (d) of 150 mm and beam thickness (b) of 80 mm. A clip-on gauge was mounted across the notch mouth lips to measure the *CMOD* (Figure 1). The loading rate was automatically adjusted via the *CMOD* feedback control to ensure stable post-peak softening capture. The full fracture process was recorded to generate the continuous *Load–CMOD* (*F–CMOD*) envelope curves [87].

The basic parameters of linear-elastic fracture mechanics (LEFM), including the K_{Ic}^{S}, $CTOD_c$, characteristic length (l_{ch}), and G_f, were evaluated using the standard international formulations provided in Table 3.

Table 3. Summary of analytical equations for fracture mechanics parameters.

Analysed parameter	Calculation equation	Reference
K_{Ic}^{S}	$K_{Ic}^{S} = 3(F_{max} + 0.5\omega)\frac{S(\pi a_c)^{1/2}F(\alpha_1)}{2d^2b}$ where: F_{max}: the measured maximum load; a_c: critical effective crack length, according to [88]; $F(\alpha_1) = \frac{1.99-\alpha_1(1-\alpha_1)(2.15-3.93\alpha_1+2.7{\alpha_1}^2)}{\sqrt{\pi^{1/2}(1+2\alpha_1)(1-\alpha_1)^{3/2}}}$ $\alpha_1 = \frac{a_c}{d}$; $\omega = \frac{W_0 S}{L}$; W_0: self weight of the beam; d, b, S, L: explained in the text	[88]
$CTOD_c$	$CTOD_c = \frac{6F_{max}Sa_cV_1(\alpha)}{Ed^2b}[(1-\beta)^2 + (1.081-9\alpha)(\beta-)]^{1/2}$ where: $\alpha = \frac{a_c}{d}$; $\beta = \frac{a_0}{a_c}$; E: Young's modulus according to [88]; $V_1(\alpha)$: is a dimensionless geometric function, dependent on α, as defined in [88]	[88]
G_f	$G_f = \frac{(A_0+mgCMOD_{failure})}{A_{lig}}$ where: A_0: the envelope area of the *F-CMOD* curve; $m = m_1 + m_2$; m_1: weight of the specimen itself; m_2: the weight of the loading head that is not secured to the machine, which is determined to be zero; g: the acceleration of gravity; $CMOD_{failure}$: deformation at the final failure of the beam; A_{lig}: area of ligament	[89]
l_{ch}	$l_{ch} = \frac{EG_f}{f_{ctm}^2}$	[90]
PDI	$PDI = \frac{W_{post}}{W_t} \times 100\%$	-

Moreover, it should be noted that for statistical reliability, 6 replicate beams and 6 cube specimens were tested for each concrete mixture, and no tests were excluded from the final analysis. The representative *F–CMOD* envelope curves were constructed by averaging the discrete load values of the replicate specimens at consistent *CMOD* intervals. To ensure an objective and uniform calculation of the W_t, the area under the *F–CMOD* curves was integrated up to a common, predefined *CMOD* endpoint of 0.3 mm for all tested specimens, corresponding to the point where the residual load capacity became negligible.

2.5. Definition and Rationale of the PDI

To assess the exact energy-absorption capacity of the concrete formulations during distinct crack propagation regimes, W_t obtained from the area under the *F–CMOD* response was mathematically bisected into two distinct physical components:

1. Pre-peak energy (W_{pre}): represented the elastic strain energy accumulated in the concrete matrix up to the point of macro-crack initiation (maximum peak load, F_{max}).

2. Post-peak energy (W_{post}): represented the work expended during the stable and unstable micro-cracking and macro-fissuring softening phase, which characterized the true residual structural capacity of the material.

The engineering rationale behind the *PDI* lies in its ability to isolate the specific contribution of the post-peak softening domain. A higher *PDI* indicates that the material retains a dominant capacity to dissipate energy via aggregate interlocking, pozzolanic ITZ bridging, and nanoparticle crack deflection after macro-cracking has initiated, preventing sudden structural cleavage. The comparative mathematical expressions for the energy components and the *PDI* are integrated within the analytical matrix of Table 3.

At this point, it should be explicitly noted that while the base formulations and preliminary compressive strength ranges of these mixtures were referenced in the author's other study [54], the entire advanced fracture mechanics campaign presented in this manuscript, including the *F–CMOD* responses, work component integrations (W_{pre}, W_{post}), and the formulation of the *PDI*, constitutes newly generated, independent data.

Furthermore, regarding the physical interpretation of these work components, it should be explicitly emphasized that for quasi-brittle cementitious materials, W_{pre} does not represent purely recoverable elastic strain energy. As demonstrated by recent mesoscale fracture investigations [91,92], concrete undergoes distributed microcracking and non-linear Fracture Process Zone (FPZ) development well before reaching the peak load. Consequently, W_{pre} encompasses recoverable elastic energy and pre-peak damage-related dissipation.

3. Results and discussion

3.1. Basic strength parameters and empirical brittleness

The foundational mechanical properties of the analyzed concrete series, including the f_{cm}, f_{ctm}, and the traditional *BI*, are summarized in Table 4.

Table 4. Average values of analyzed basic strength parameters with coefficients of variations (COV).

Analyzed parameter	Mix No.			
	REF	NSF	H1	H2
f_{cm} (MPa)–%, COV (%)	38.32–100, 5.80	53.89–140.63, 6.87	56.87–148.41, 7.22	50.12–130.79, 7.28
f_{ctm} (MPa)–%, COV (%)	2.90–100, 6.72	4.02–138.62, 7.08	4.26–146.90, 7.35	3.76–129.66, 7.40
BI (-)–%, COV (-)	7.57–100, -	7.46–98.55, -	7.49–98.94, -	7.50–99.08, -

The introduction of the highly reactive NS and SF in the ternary NSF mix significantly increased the f_{cm} by over 40% compared to the REF concrete. The highest mechanical performance was recorded for the quaternary H1 mix, achieving an f_{cm} of 56.87 MPa (a 48.4% increase relative to REF). Similarly, the splitting tensile strength reached its peak in the H1 series at 4.26 MPa (Table 4). Despite these substantial strength gains, the classical *BI* values remained relatively stagnant, hovering between 7.46 and 7.57 across all modified series [93,94]. This minimal variation in *BI* falsely suggests that the brittleness of the material is unaffected by the profound microstructural densification caused by the

nanoadditives. This highlights the severe limitations of using solely static strength ratios to evaluate the structural safety of high-performance hybrid concretes [95–97], necessitating a deeper non-linear fracture mechanics approach [98–100].

3.2. F–CMOD envelope curves and fracture energy components

The continuous fracture process and energy dissipation capabilities of the concrete composites are best illustrated through the *F–CMOD* envelope curves (Figure 2) and the corresponding quantitative fracture parameters detailed in Table 5. In addition, Figure 3 shows a detailed graphical representation of the fracture energy evolution and post-peak softening behavior for the analyzed concrete mixes.

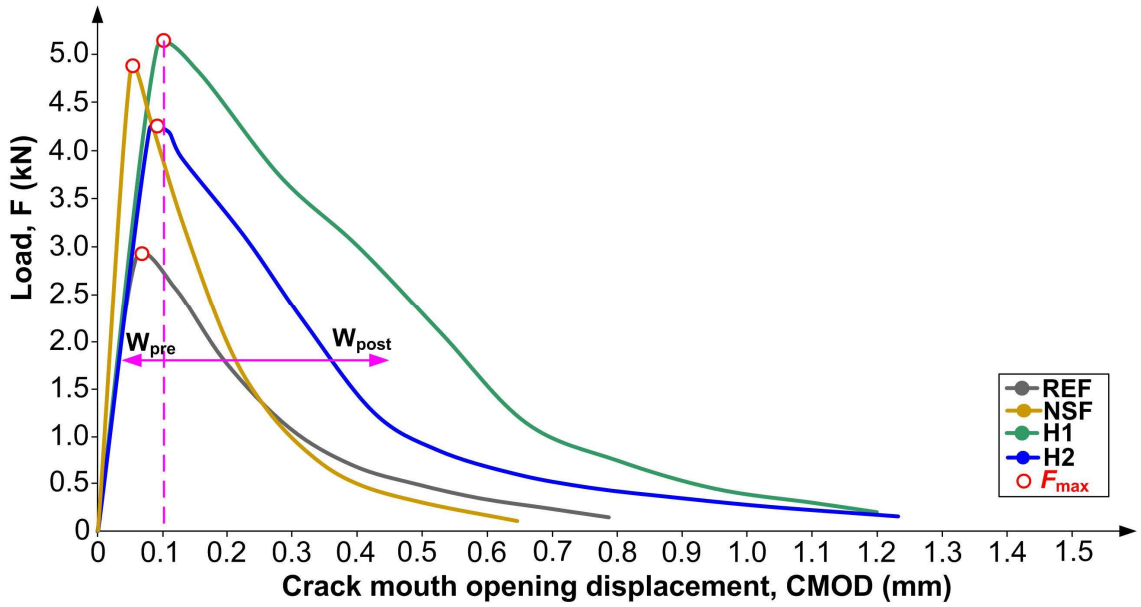


Figure 2. Experimental *F–CMOD* envelope curves illustrating the full fracture process for all concrete mixes.

Table 5. Average values of fracture mechanics parameters with COV.

Analyzed parameter	Mix No.			
	REF	NSF	H1	H2
K_{Ic}^{S} (MNm$^{-3/2}$)–%, COV (%)	1.06–100, 8.31	1.50–141.51, 9.02	1.58–149.10, 9.35	1.39–131.13, 9.52
$CTOD_c$ (m × 10^{-6})–%, COV (%)	10.41–100, 9.14	14.78–141.98, 10.27	15.64–150.24, 10.53	13.68–131.41, 10.62
G_f (N/m)–%, COV (%)	102.37–100, 15.14	136.31–133.15, 16.28	196.87–192.31, 16.55	201.40–196.74, 16.61
l_{ch} (mm)–%, COV (%)	360.21–100, -	311.03–86.35, -	430.34–119.47, -	506.33–140.57, -
W_{pre} (J)–%, COV (%)	0.089–100, 14.82	0.125–140.45, 15.94	0.207–232.58, 16.08	0.195–219.10, 16.23
W_{post} (J)–%, COV (%)	0.729–100, 14.96	0.709–97.26, 16.02	1.805–247.60, 16.12	1.353–185.60, 16.30
W_t (J)–%, COV (%)	0.818–100, 14.88	0.834–101.96, 15.97	2.012–245.96, 16.11	1.548–189.24, 16.27
PDI (-)–%, COV (%)	89.12–100, 1.44	85.01–95.39, 1.16	89.71–100.66, 1.94	87.40–98.07, 1.68

It is important to emphasize that while absolute thermodynamic fracture energy is traditionally calculated by integrating load with load-point deflection (*LPD*), the areas calculated in this study are derived from the *F–CMOD* curves. This represents a *CMOD*-based fracture work equivalent. The mechanical justification for this approach is that *CMOD* is strictly sensitive to the local crack separation and the cohesive bridging within the FPZ, effectively filtering out extraneous deformations such as support crushing and machine compliance.

Based on the above, it was found that the reference concrete exhibited a typical, relatively low peak load and a distinct softening tail. The incorporation of NS and SF (NSF series) drastically increased F_{max} and W_{pre}, which rose from 0.089 J (REF) to 0.125 J (NSF). However, W_{post} for the NSF mix slightly decreased to 0.709 J, indicating that while the matrix became significantly stronger, it also became more brittle after crack initiation.

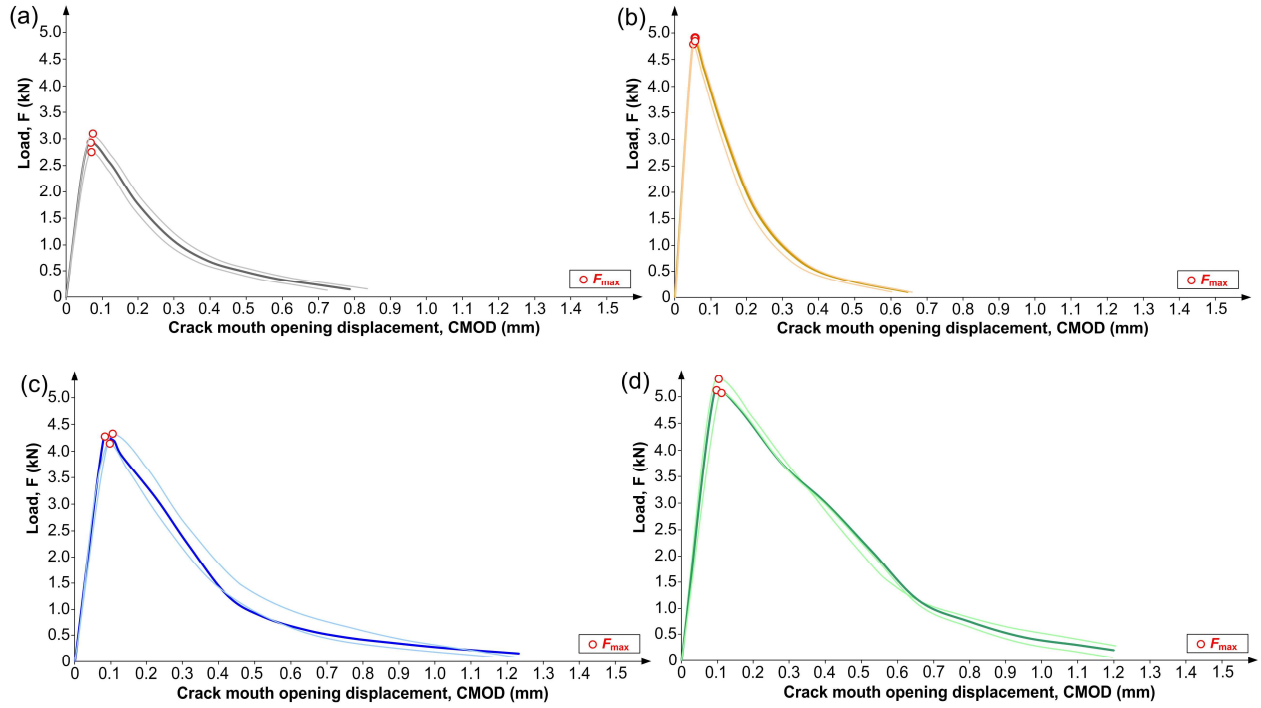


Figure 3. Detailed graphical representation of the W_{pre} and W_{post} fracture work decomposition and the resulting *PDI* trend for the analyzed concrete mixes: (a) REF; (b) NSF; (c) H1; (d) H2.

As illustrated in the newly added Figure 3 and detailed in Table 5, the *PDI* values were calculated individually for each specimen to evaluate statistical reliability. Although the absolute fracture work components (W_{pre} and W_{post}) exhibited normal scatter (COV approx 15%–16%), the resulting *PDI* showed very low dispersion across all mixes (COV < 2.0). This confirms that the proportion of post-peak energy absorption is a highly consistent structural property. While the shift from 85.01% (REF) to 89.71% (H1) represents a modest numerical increment, physically it marks a clear enhancement in the post-peak softening tail, reflecting superior crack-bridging capability induced by the hybrid nano- and micro-fillers.

This detrimental brittleness effect was reversed in the hybrid quaternary systems. The H1 and H2 mixes exhibited a massive synergy between NS, SF, and FA. As shown in the energy distribution

analysis (Figure 4a), the W_t explicitly exploded in the H1 series, reaching 2.012 J; an outstanding 145.9% increase compared to the reference mix. Most notably, the component W_{post} in H1 reached 1.805 J. This phenomenon likely proves that the combined presence of FA and NS effectively bridges micro-cracks and provides immense resistance to crack propagation in the softening phase. Consequently, the normalized total G_f nearly doubled, jumping from 102.37 N/m in the REF concrete to over 201 N/m in the H2 formulation (Table 5).

The evaluation of the novel *PDI* index revealed the true physical nature of the material's failure (Figure 4b). The NS mix recorded the lowest *PDI* (85.01%), reflecting its higher relative brittleness. Conversely, the H1 and H2 formulations managed to restore the improved fracture resistance levels characteristic of ordinary concrete, achieving *PDI* values of 89.71% and 87.40%, respectively. This proved that the proposed hybrid SCM modification enables the design of a composite that is simultaneously extremely strong and characterized by reduced brittleness.

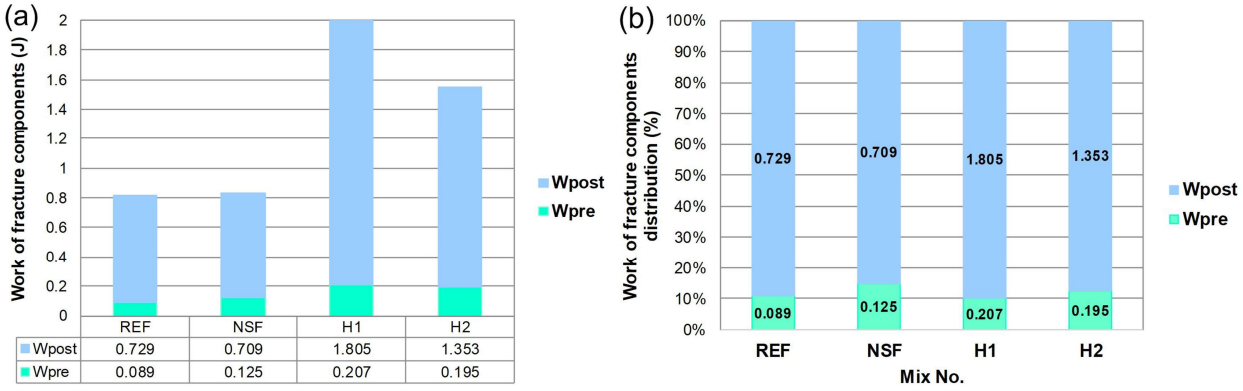


Figure 4. Analysis of the fracture work components for the tested concrete mixes: (a) absolute values of W_{pre} and W_{post} fracture energy; (b) percentage distribution of the fracture work components.

3.3. Multi-criteria radar chart evaluation

To synthetically compare the holistic performance of the developed composites, a multi-criteria radar chart was constructed (Figure 5). All values were normalized to the reference concrete (REF = 1.0). The visual profile demonstrates that the quaternary mixtures (H1 and H2) dominate the outer boundaries of the chart, particularly pulling the material behavior toward exceptionally high K_{Ic}^{S} and G_f. The radar chart simultaneously shows that while the standard *BI* slightly shrinks toward the center (suggesting theoretical improvement), the true post-peak safety margin remains exceptionally high and stable, as evidenced by the *PDI* axis remaining close to the 1.0 threshold.

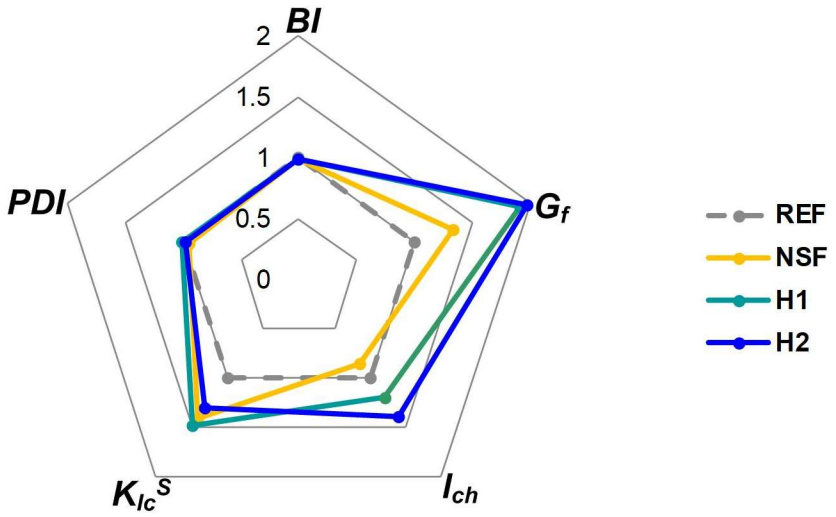


Figure 5. Radar chart presenting a multi-criteria evaluation of the mechanical and fracture mechanics parameters of the analyzed concrete mixes, normalized to the REF.

3.4. Pearson correlation matrix analysis

The comprehensive Pearson correlation matrix (Table 6) provides the statistical validation for the introduced parameters. Positive correlations ($r > 0.99$) were observed between the fundamental strength parameters (f_{cm}, f_{ctm}) and critical LEFM indicators such as K_{Ic}^S and $CTOD_c$. Crucially, the statistical analysis validated the necessity of the *PDI* framework. Moreover, the traditional *BI* exhibited negative correlations with W_t, $r = -0.274$ and W_{post}, $r = -0.248$. This mathematically proved that a lower *BI* does not reliably guarantee higher energy absorption during catastrophic failure. In contrast, W_{post} display near-perfect linear correlations with G_f, $r = 0.879$ and W_t, $r = 0.999$, confirming that the newly proposed *PDI* metric accurately tracks the non-linear, physical crack-resistance capabilities of sustainable concrete.

Table 6. Pearson correlation matrix of the evaluated concrete properties.

Variables	f_{cm}	f_{ctm}	*BI*	K_{Ic}^S	$CTOD_c$	G_f	l_{ch}	W_{pre}	W_{post}	W_t	*PDI*
f_{cm}	1										
f_{ctm}	0.999871	1									
BI	–0.91349	–0.90702	1								
K_{Ic}^S	0.999967	0.999722	–0.91599	1							
$CTOD_c$	0.999933	0.999844	–0.91137	0.999922	1						
G_f	0.713622	0.721191	–0.51168	0.708329	0.708962	1					
l_{ch}	0.164429	0.174829	0.036244	0.157096	0.157634	0.808001	1				
W_{pre}	0.737075	0.745671	–0.49738	0.731698	0.7338	0.991774	0.773011	1			
W_{post}	0.597407	0.60997	–0.24818	0.591146	0.597634	0.879055	0.720814	0.92747	1		
W_t	0.614746	0.627005	–0.27391	0.60853	0.614635	0.895577	0.730464	0.940407	0.999344	1	
PDI	–0.25629	–0.24122	0.627374	–0.26225	–0.25129	0.144223	0.392244	0.223946	0.550511	0.522376	1

4. Conclusions

Based on the comprehensive multi-criteria experimental investigation of hybrid cementitious composites modified with nanosilica, silica fume, and siliceous fly ash, the following primary conclusions can be drawn:

- Combined strength and toughness: the quaternary hybrid mixture containing 5% NS, 10% SF, and 5% FA (mix H1) provides the optimal balance of static strength and dynamic fracture toughness. It achieved a 48% increase in compressive strength alongside a dramatic 145% increase in the W_t compared to the reference concrete.
- Dominance of post-peak energy: the mathematical bisection of the *F–CMOD* envelope curves proved that the absolute majority of energy dissipation occurs in the post-cracking softening phase. For the optimal hybrid mixes, W_{post} constituted up to 89.7% of the G_f.
- Validation of the novel *PDI* parameter: the newly introduced *PDI* successfully captured the nuanced shifts in material brittleness that traditional static indices (like *BI*) failed to detect. While the sole addition of NS decreased the *PDI* to 85.01%, the inclusion of FA effectively restored it, likely confirming FA's crucial role in micro-crack bridging and post-peak stabilization.
- Statistical independence of ductility: the Pearson correlation matrix confirmed that traditional brittleness indices correlate negatively with the actual non-linear work of fracture. The *PDI* and its constituent energy parameters (W_{pre}, W_{post}) serve as a far more reliable, structurally accurate framework for assessing the true catastrophic failure resistance of high-performance eco-concretes.

Use of AI tools declaration

The author declares that no artificial intelligence (AI) tools were used in the creation of this article.

Acknowledgments

This work was financially supported by the Ministry of Education and Science of the Republic of Poland within the statutory research numbers: FD-20/IL-4/017.

Conflict of interest

Grzegorz Ludwik Golewski is on a special issue editorial board for *AIMS Materials Science* and was not involved in the editorial review or the decision to publish this article. The author declares no conflict of interest.

References

1. Amran M, Onaizi AM, Qader DN, et al. (2022) Innovative use of fly ash-finely powdered glass cullet as a nano additives for a sustainable concrete: Strength and microstructure and cost analysis. *Case Stud Constr Mat* 17: e01688. https://doi.org/10.1016/j.cscm.2022.e01688
2. Abood AM, Khazal H, Hassan AF (2022) On the determination of first-mode stress intensity factors and T-stress in a continuous functionally graded beam using digital image correlation method. *AIMS Mater Sci* 9: 56–70. https://doi.org/10.3934/matersci.2022004

3. Golewski GL (2022) The specificity of shaping and execution of monolithic pocket foundations (PF) in hall buildings. *Buildings* 12: 192. https://doi.org/10.3390/buildings12020192
4. Benhelal E, Zahedi G, Shamsaei E, et al. (2013) Global strategies and potentials to curb CO_2 emissions in cement industry. *J Clean Prod* 51: 142–161. https://doi.org/10.1016/j.jclepro.2012.10.049
5. Voldsund M, Gardarsdottir SO, De Lena E, et al. (2019) Comparison of technologies for CO_2 capture from cement production–Part 1: Technical evaluation. *Energies* 12: 559. https://doi.org/10.3390/en12030559
6. Riaz Ahmad M, Fernàndez-Jimenez A, Chen B, et al. (2024) Low-carbon cementitious materials: Scale-up potential, environmental impact and barriers. *Constr Build Mater* 445: 139087. https://doi.org/10.1016/j.conbuildmat.2024.139087
7. Marandi N**,** Shirzad S (2025) Sustainable cement and concrete technologies: a review of materials and processes for carbon reduction. *Innov Infrastruct Solut* 10: 408. https://doi.org/10.1007/s41062-025-02213-5
8. Bao S, Xie T, Chen H, et al. (2026) Synergistic effects of ultra-fine fly ash, silica fume and micro-nano bubble water on fracture properties of fly ash mortars. *J Build Eng* 123: 115944. https://doi.org/10.1016/j.jobe.2026.115944
9. Aprianti SE (2017) A huge number of artificial waste material can be supplementary cementitious material (SCM) for concrete production—A review part II. *J Clean Prod* 142: 4178–4194. https://doi.org/10.1016/j.jclepro.2015.12.115
10. Xie T, Visitin P (2018) A unified approach for mix design of concrete containing supplementary cementitious materials based on reactivity moduli. *J Clean Prod* 203: 68–82. https://doi.org/10.1016/j.jclepro.2018.08.254
11. Xie T, Yang G, Zhao X, et al. (2020) A unified model for predicting the compressive strength of recycled aggregate concrete containing supplementary cementitious materials. *J Clean Prod* 251: 119752. https://doi.org/10.1016/j.jclepro.2019.119752
12. Zhang J, Ke G, Liu Y (2021) Early hydration heat of calcium sulfomluminate cement with lnfluences of supplementary cementitious materials and water to binder ratio. *Materials* 14: 642. https://doi.org/10.3390/ma14030642
13. Yaseen N, Alcivar-Bastidas S, Irfan-ul-Hassan M, et al. (2024) Concrete incorporating supplementary cementitious materials: Temporal evolution of compressive strength and environmental life cycle assessment. *Heliyon* 10: e25056. https://doi.org/10.1016/j.heliyon.2024.e25056
14. Ahmed A (2024) Assessing the effects of supplementary cementitious materials on concrete properties: A review. *Disc Civ Eng* 1: 145. https://doi.org/10.1007/s44290-024-00154-z
15. Torres-Acosta AA, Méndez-Páramo RA, Arista-Perrusquía C, et al. (2025) Portland cement paste performance when inert limestone filler is added as clinker replacement. *AIMS Mater Sci* 12: 224–244. https://doi.org/10.3934/matersci.2025012
16. Piyarat N, Wangrakdiskul U, Maingam P (2021) Investigations of the influence of various industrial waste materials containing rice husk ash, waste glass, and sediment soil for eco-friendly production of non-fired tiles. *AIMS Mater Sci* 8: 469–485. https://doi.org/10.3934/matersci.2021029

17. Abdulrahman H, Muhamad R, Visitin P, et al. (2022) Mechanical properties and bond stress-slip behaviour of fly ash geopolymer concrete. *Constr Build Mater* 327: 126909. https://doi.org/10.1016/j.conbuildmat.2022.126909
18. Azizi M, Samimi K (2025) Effect of silica fume on self-compacting earth concrete: Compressive strength, durability and microstructural studies. *Constr Build Mater* 472: 140815. https://doi.org/10.1016/j.conbuildmat.2025.140815
19. Lv X, Shi Y, Zhou S (2025) Effects of fly ash and silica fume on abrasion resistance of high-ferrite Portland cement: A comparative study. *Constr Build Mater* 489: 142198. https://doi.org/10.1016/j.conbuildmat.2025.142198
20. Hamada HM, Abed F, Binti Katman HY, et al. (2023) Effect of silica fume on the properties of sustainable cement concrete. *J Mater Res Techn* 24: 8887–8908. https://doi.org/10.1016/j.jmrt.2023.05.147
21. Wang L, Zhang P, Guan J, et al. (2023) Editorial: Fabrication and properties of concrete containing industrial waste. *Front Mater* 10: 1169715. https://doi.org/10.3389/fmats.2023.1169715
22. Kim Y, Hanif A, Usman M, et al. (2018) Slag waste incorporation in high early strength concrete as cement replacement: Environmental impact and influence on hydration & durability attributes. *J Clean Prod* 172: 3056–3065. https://doi.org/10.1016/j.jclepro.2017.11.105
23. Han F, Pu S, Zhou Y, et al. (2021) Effect of ultrafine mineral admixtures on the rheological properties of fresh cement paste: A review. *J Build Eng* 51: 104313. https://doi.org/10.1016/j.jobe.2022.104313
24. Karlina AI, Karlina YI, Gladkich VA (2023) Analysis of experience in the use of micro- and nanoadditives from silicon production waste in concrete technologies. *Minerals* 13: 1525. https://doi.org/10.3390/min13121525
25. Abhilash PP, Kumar Nayak D, Sangoju B, et al. (2021) Effect of nano-silica in concrete: A review. *Constr Build Mater* 278: 122347. https://doi.org/10.1016/j.conbuildmat.2021.122347
26. Ahmadi SH, Mazloom M, Salehi H (2024) Total and initial fracture energies of self-compacting lightweight concrete containing silica fume and nano-silica. *Eng Fract Mech* 308: 110382. https://doi.org/10.1016/j.engfracmech.2024.110382
27. Sanjuán MA, Argiz C, Galvez JC, et al. (2018) Combined effect of nano-SiO_2 and nano-Fe_2O_3 on compressive strength, flexural strength, porosity and electrical resistivity in cement mortars. *Mater De Constr* 68: e150. https://doi.org/10.3989/mc.2018.10716
28. Golewski GL, Xi X, Zheng Y, et al. (2025) Experimental evaluation of Mode II fracture and microstructure of matrix-aggregate bond of concrete with crushed limestone. *C Stud Constr Mater* 23: e05183. https://doi.org/10.1016/j.cscm.2025.e05183
29. Oltulu M, Sahin R (2023) Effect of nano-SiO_2, nano-Al_2O_3 and nano-Fe_2O_3 powders on compressive strengths and capillary water absorption of cement mortar containing fly ash: A comparative study. *Ener Build* 58: 292–301. https://doi.org/10.1016/j.enbuild.2012.12.014
30. Prokopski G, Halbiniak J (2000) Interfacial transition zone in cementitious materials. *Cem Concr Res* 30: 579–583. https://doi.org/10.1016/S0008-8846(00)00210-6
31. Golewski GL (2025) The investigation of shear fracture toughness and structure of ITZ of limestone concrete with different aggregate grain size. *Materials* 18: 3954. https://doi.org/10.3390/ma18173954

32. Joshaghani A, Balapour M, Moshhadian M, et al. (2020) Effects of nano-TiO_2, nano-Al_2O_3, and nano-Fe_2O_3 on rheology, mechanical and durability properties of self-consolidating concrete (SCC): An experimental study. *Constr Build Mater* 245*:* 1118444. https://doi.org/10.1016/j.conbuildmat.2020.118444
33. Peng Y, Ma K, Long G, et al. (2019) Influence of nano-SiO_2, nano-$CaCO_3$ and nano-Al_2O_3 on rheological properties of cement-fly ash paste. *Materials* 12: 2598. https://doi.org/10.3390/ma12162598
34. Siang Ng D, Paul SC, Anggraini V, et al. (2020) Influence of SiO_2, TiO_2 and Fe_2O_3 nanoparticles on the properties of fly ash blended cement mortars. *Constr Build Mater* 258: 119627. https://doi.org/10.1016/j.conbuildmat.2020.119627
35. Imam A, Sharma KK, Kumar V, et al. (2022) A review study on sustainable development of ultra high-performance concrete. *AIMS Mater Sci* 9: 9–35. https://doi.org/10.3934/matersci.2022002
36. Singh RP, Vanapalli KR, Jadda K, et al. (2024) Durability assessment of fly ash, GGBS, and silica fume based geopolymer concrete with recycled aggregates against acid and sulfate attack. *J Build Eng* 82: 108354. https://doi.org/10.1016/j.jobe.2023.108354
37. Alperen Bulut H, Sahin R (2022) Radiological characteristics of self-compacting concretes incorporating fly ash, silica fume, and slag. *J Build Eng* 58: 104987. https://doi.org/10.1016/j.jobe.2022.104987
38. Mohseni E, Miyandehi BM, Yang J, et al. (2015) Single and combined effects of nano-SiO_2, nano-Al_2O_3 and nano-TiO_2 on the mechanical, rheological and durability properties of self-compacting mortar containing fly ash. *Constr Build Mater* 84: 331–340. https://doi.org/10.1016/j.conbuildmat.2015.03.006
39. Xi X, Zheng Y, Zhuo J, et al. (2024) Influence of water glass modulus and alkali content on the properties of alkali-activated thermally activated recycled cement. *Constr Build Mater* 452: 138867. https://doi.org/10.1016/j.conbuildmat.2024.138867
40. Xi X, Zheng Y, Zhuo J, et al. (2024) Mechanical properties and hydration mechanism of nano-silica modified alkali-activated thermally activated recycled cement. *J Build Eng* 98: 110998. https://doi.org/10.1016/j.jobe.2024.110998
41. Falikman V (2022) Defined-performance concretes using nanomaterials and nanotechnologies. *Eng Proc* 17: 12. https://doi.org/10.3390/engproc2022017012
42. Zhang P, Han S, Wang X, et al. (2020) Nanoparticle-reinforced building materials with applications in civil engineering. *Adv Mech Eng* 12: 1–4. https://doi.org/10.1177/1687814020965438
43. Tasdemir C, Tasdemir MA, Lydon FD, et al. (1996) Effects of silica fume and aggregate size on the brittleness of concrete. *Cem Concr Res* 26: 63–68. https://doi.org/10.1016/0008-8846(95)00180-8
44. Ahmad J, Abid SR, Arbili MM, et al. (2022) A review on sustainable concrete with the partially substitutions of silica fume as a cementitious material. *Sustainability* 14: 12075. https://doi.org/10.3390/su141912075
45. Alex AG, Kemal Z, Gebrehiwet T, et al. (2022) Effect of α: Phase nano Al_2O_3 and rice husk ash in cement mortar. *Adv Civ Eng* 2022: 4335736. https://doi.org/10.1155/2022/4335736
46. Land G, Stephan D (2012) The influence of nano-silica on the hydration of ordinary Portland cement. *J Mater Sci* 47: 1011–1017. https://doi.org/10.1007/s10853-011-5881-1

47. Chen S, Wang H, Guan J, et al. (2022) Determination method and prediction model of fracture and strength of recycled aggregate concrete at different curing ages. *Constr Build Mater* 343: 128070. https://doi.org/10.1016/j.conbuildmat.2022.128070
48. Zhang S, Han B, Xie H, et al. (2021) Brittleness of concrete under different curing conditions. *Materials* 14: 7865. https://doi.org/10.3390/ma14247865
49. Raphael JM (1984) Tensile strength of concrete. *ACI Mater J* 81: 158–165. https://doi.org/10.14359/10653
50. Oluokun FA (1991) Prediction of concrete tensile strength from compressive strength: evaluation of existing relations for normal weight concrete. *ACI Mater J* 88: 302–309. https://doi.org/10.14359/1942
51. Biricik H, Sarier N (2014) Comparative study of the characteristics of nanosilica–, silica fume– and fly ash–incorporated cement mortars. *Mater Res* 17: 570–582. https://doi.org/10.1590/S1516-14392014005000054
52. El-Fekyl MS, Youssef P, El-Tair AM, et al. (2019) Effect of nano silica addition on enhancing the performance of cement composites reinforced with nano cellulose fibers. *AIMS Mater Sci* 6: 864–883. https://doi.org/10.3934/matersci.2018.6.864
53. Han F, Pu S, Zhou Y, et al. (2022) Effect of ultrafine mineral admixtures on the rheological properties of fresh cement paste: A review. *J Build Eng* 51: 104313. https://doi.org/10.1016/j.jobe.2022.104313
54. Golewski GL (2023) Mechanical properties and brittleness of concrete made by combined fly ash, silica fume and nanosilica with ordinary Portland cement. *AIMS Mater Sci* 10: 390–404. https://doi.org/10.3934/matersci.2023021
55. Kaźmierowski M, Siemiginowski M, Kordasz M, et al. (2026) Compressive deformability and flexural fracture energy of high-strength concrete with bamboo fibers. *Sci Rep* 16: 18341. https://doi.org/10.1038/s41598-026-48624-x
56. Craciun EM (2008) Energy criteria for crack propagation in prestresses elastic composites. *Sol Mech Appl* 154: 193–237. https://doi.org/10.1007/978-1-4020-8772-1_7
57. Golewski GL (2024) Effect of coarse aggregate type on the fracture toughness of ordinary concrete. *Infrastructures* 11: 105509. https://doi.org/10.3390/infrastructures9100185
58. Guan J, Yin Y, Li Y, et al. (2022) A design method for determining fracture toughness and tensile strength pertinent to concrete sieving curve. *Eng Fract Mech* 271: 108596. https://doi.org/10.1016/j.engfracmech.2022.108596
59. Wu J, Yang J, Zhang R, et al. (2022) Fatigue life estimating for chloride attacked RC beams using S-N curve combined with mesoscale simulation of chloride ingress. *Int J Fat* 158: 106751. https://doi.org/10.1016/j.ijfatigue.2022.106751
60. Guan J, Zhang Y, Meng J, et al. (2022) A simple method for determining independent fracture toughness and tensile strength of rock. *Int J Min Sci Technol* 32: 707–726. https://doi.org/10.1016/j.ijmst.2022.05.004
61. Kim JK, Lee CS, Park CK, et al. (1997) The fracture characteristics of crushed limestone sand concrete. *Cem Concr Res* 27: 1719–1729. https://doi.org/10.1016/S0008-8846(97)00156-7
62. Wan C, Hou P, Zhou L, et al. (2026) The fracture performance of modified recycled concrete: Influence of recycled aggregate and recycled powder. *Eng Fract Mech* 331: 111709. https://doi.org/10.1016/j.engfracmech.2025.111709
63. Miannay DP (1998) *Fracture Mechanics*, New York: Springer-Verlag.

64. Prokopski G, Langier B (2000) Effect of water/cement ratio and silica fume addition on the fracture toughness and morphology of fractured surfaces of gravel concretes. *Cem Concr Res* 30: 1427–1433. https://doi.org/10.1016/S0008-8846(00)00332-X
65. Kim JK, Lee CS, Ho SH (1997) The fracture characteristics of crushed limestone sand concrete. *Cem Concr Res* 27: 1719–1729. https://doi.org/10.1016/S0008-8846(97)00156-7
66. Giaccio G, Rocco C, Zorbino R (1993) The fracture energy (GF) of high-strength concretes. *Mater Struct* 26: 381–386. https://doi.org/10.1007/BF02472938
67. Fakoor M, Shahsavar S (2021) The effect of T-stress on mixed mode I/II fracture of composite materials: Reinforcement isotropic solid model in combination with maximum shear stress theory. *Int J Sol Struct* 229: 111145. https://doi.org/10.1016/j.ijsolstr.2021.111145
68. Zhang P, Gao JX, Dai XB, et al. (2016) Fracture behavior of fly ash concrete containing silica fume. *Struct Eng Mech* 59: 261–275. https://doi.org/10.12989/sem.2016.59.2.261
69. Figueiredo F, da Silva P, Rotero ER, et al. (2022) Concrete with partial replacement of natural aggregate by PET aggregate—An exploratory study the influence in the compressive strength. *AIMS Mater Sci* 9: 172–183. https://doi.org/10.3934/matersci.2021022
70. Golewski GL (2025) A new concrete composites based on quaternary binder systems reinforced nanosilica with enhanced fracture toughness and reduced interfacial microcracks. *Adv Nano Res* 19: 545–557. https://doi.org/10.12989/anr.2025.19.6.545
71. Dave N, Misra AK, Srivastava A, et al. (2017) Study on quaternary micro-structure, strength, durability considering the influence of multi-factors. *Constr Build Mater* 139: 447–457. https://doi.org/10.1016/j.conbuildmat.2017.02.068
72. Dave N, Misra AK, Srivastava A, et al. (2017) Setting time and standard consistency of quaternary binders: The influence of cementitious material addition and mixing. *Int J Sustain Built Environ* 6: 30–36. https://doi.org/10.1016/j.ijsbe.2016.10.004
73. Dave N, Misra AK, Srivastava A, et al. (2016) Experimental analysis of strength and durability properties of quaternary cement binder and mortar. *Constr Build Mater* 107: 117–124. https://doi.org/10.1016/j.conbuildmat.2015.12.195
74. Li LG, Zheng JY, Ng PL, et al. (2021) Synergistic cementing efficiencies of nano-silica and micro-silica in carbonation resistance and sorptivity of concrete. *J Build Eng* 33: https://doi.org/101862.10.1016/j.jobe.2020.101862
75. EN 197-1:2011 (2011) Cement—Part 1: Composition, specifications and conformity criteria for common cements. NSAI Standard: Dublin, Ireland.
76. ASTM C 618-03 (2008) Standard specification for coal fly ash and raw or calcined natural pozzolan for use in concrete. Annual book of ASTM standard: West Conshohocken, PA, USA.
77. EN 1008:2002 (2002) Mixing water for concrete—specification for sampling, testing and assessing the suitability of water, including water recovered from processes in the concrete industry, as mixing water for concrete. British Standards Institution (BSI): London, UK.
78. Fraay ALA, Bijen JM, de Haan YM (1989) The reaction of fly ash in concrete. A critical examination. *Cem Concr Res* 19: 235–246. https://doi.org/10.1016/0008-8846(89)90088-4
79. Odler I (1991) Strength of cement (final report). *Mater Struct* 24: 143–157. https://doi.org/10.1007/BF02472476
80. Ho DWS, Lewis RK (1985) Effectiveness of fly ash for strength and durability of concrete. *Cem Concr Res* 15: 793–800. https://doi.org/10.1016/0008-8846(85)90145-0

81. Zhang MH (1995) Microstructure, crack propagation, and mechanical properties of cement pastes containing high volumes of fly ashes. *Cem Concr Res* 25: 1165–1178. https://doi.org/10.1016/0008-8846(95)00109-P
82. DIN 4226-1:2001-07 (2001) Aggregates for concrete and mortar—Part 1: Normal and heavy-weight aggregates. German Standards Institution: Essen, Germany.
83. EN 13791:2019-12 (2019) Assessment of in-situ compressive strength in structures and precast concrete components. British Standards Institution (BSI): London, UK.
84. EN 12390-2:2019 (2019) Testing hardened concrete—Part 2: Making and curing specimens for strength tests. British Standards Institution (BSI): London, UK.
85. EN 12390-3:2011+AC (2012) Testing hardened concrete—Part 3: Compressive strength of test specimens. British Standards Institution (BSI): London, UK.
86. EN 12390-6:2009 (2009) Testing hardened concrete—Part 6: Tensile Splitting strenght of test specimens. British Standards Institution (BSI): London, UK.
87. Golewski GL (2024) Comparison of fracture behavior of set concretes based on natural and crushed aggregates. *Mater Res Express* 11: 105509. https://doi.org/10.1088/2053-1591/ad87b4
88. Shah SP (1990) Determination of fracture parameters (K_{Ic}^{S} and $CTOD_c$) of plain concrete using three-point bend tests. *Mater Struct* 23: 457–460. https://doi.org/10.1007/BF02472029
89. RILEM TC 50-FMC (1985) Determination of the fracture energy of mortar and concrete by means of three-point bend tests on notched beams. *Mater Struct* 18: 285–290. https://doi.org/10.1007/BF02472918
90. Hillerborg A, Modéer M, Petersoon PE (1976) Analysis of crack formation and crack growth in concrete by means of fracture mechanics and finite elements. *Cem Concr Res* 6: 773–782. https://doi.org/10.1016/0008-8846(76)90007-7
91. Zhou R, Lu Y, Wang LG, et al. (2021) Mesoscale modelling of size effect on the evolution of fracture process zone in concrete. *Eng Fract Mech* 252: 107559. https://doi.org/10.1016/j.engfracmech.2021.107559
92. Zhou R, Chen HM (2019) Mesoscopic investigation of size effect in notched concrete beams: The role of fracture process zone. *Eng Fract Mech* 213: 103–118. https://doi.org/10.1016/j.engfracmech.2019.03.028
93. Behfarnia M, Salemi O (2017) Combined effects of micro-silica and nano-silica on durability of mortar. *Constr Build Mater* 157: 337–347. https://doi.org/10.1016/j.conbuildmat.2017.09.105
94. Wang Y, Xu Z, Wang J, et al. (2020) Synergistic effect of nano-silica and silica fume on hydration properties of cement-based materials. *J Ther Anal Calorim* 140: 2225–2235. https://doi.org/10.1007/s10973-019-08929-8
95. Liu M, Tan H, He X (2014) Effect of nano-silica on early strength and microstructure of fly ash concrete. *Constr Build Mater* 52: 300–306. https://doi.org/10.1016/j.conbuildmat.2018.10.214
96. Li G (2004) Properties of high-volume fly ash concrete incorporating nano-SiO_2. *Cem Concr Res* 34: 1043–1049. https://doi.org/10.1016/j.cemconres.2003.11.013
97. Zhang P, Li Q (2013) Effect of polypropylene fiber on durability of concrete composite containing fly ash and silica fume. *Compos Part B Eng* 45: 1587–1594. https://doi.org/10.1016/j.compositesb.2012.10.006
98. Hou PK, Kawashima S, Wang KJ, et al. (2013) Effects of colloidal nanosilica on rheological and mechanical properties of fly ash-cement mortar. *Cem Concr Compos* 35: 12–22. https://doi.org/10.1016/j.cemconcomp.2012.08.027

99. Mehrab AH, Yaqubi E, Amirfakhrian S, et al. (2025) Multidimensional fracture assessment of SCM-modified high-performance hybrid fiber-reinforced concrete: Comparative insights from WFM, SEM, and BEM approaches. *Res Eng* 28: 107800. https://doi.org/10.1016/j.rineng.2025.107800
100. Kaur Sood S, Vesmawala GR (2024) An overview of recent advances in fracture performance of nano engineered cement composites. *Constr Build Mater* 431: 136489. https://doi.org/10.1016/j.conbuildmat.2024.136489



AIMS Press

© 2026 the Author(s), licensee AIMS Press. This is an open access article distributed under the terms of the Creative Commons Attribution License (http://creativecommons.org/licenses/by/4.0)